Research Square

Preprints are preliminary reports that have not undergone peer review.
They should not be considered conclusive, used to inform clinical practice,
or referenced by the media as validated information.

Evaluation of passive radio sounding of icy moons based on a radar equation

Ayuto Kawakami

kawakami.ayuto.r2@dc.tohoku.ac.jp

Tohoku University: Tohoku Daigaku https://orcid.org/0009-0000-6330-144X

Yasumasa Kasaba

Tohoku University: Tohoku Daigaku

Atsushi Kumamoto

Tohoku University: Tohoku Daigaku

Fuminori Tsuchiya

Tohoku University: Tohoku Daigaku

Emi Tanaka

Tohoku University: Tohoku Daigaku

Research Article

Keywords: passive radar sounding, planetary radio emission, Moon, Ganymede, icy moons, JUICE, Kaguya

Posted Date: November 9th, 2026

DOI: https://doi.org/10.21203/rs.3.rs-11365634/v1

License: This work is licensed under a Creative Commons Attribution 4.0 International License.
Read Full License

Additional Declarations:
Figure 22 is not available with this version

Title: Evaluation of passive radio sounding of icy moons based on a radar equation

Author #1: Ayuto Kawakami, Graduate School of Science, Tohoku University, Sendai, Japan, kawakami.ayuto.r2@dc.tohoku.ac.jp (Corresponding author)
Author #2: Yasumasa Kasaba, Graduate School of Science, Tohoku University, Sendai, Japan, kasaba.y@tohoku.ac.jp
Author #3: Atsushi Kumamoto, Graduate School of Science, Tohoku University, Sendai, Japan, atsushi.kumamoto.b1@tohoku.ac.jp
Author #4: Fuminori Tsuchiya, Graduate School of Science, Tohoku University, Sendai, Japan, tsuchiya.f@tohoku.ac.jp
Author #5: Emi Tanaka, Graduate School of Science, Tohoku University, Sendai, Japan

Abstract

Passive radar sounding is one of the ways to observe surfaces and subsurfaces of planetary objects through reflection of natural radio emissions. Using observations of Radio and Plasma Investigations (RPWI) aboard Jupiter Icy Moons Explorer (JUICE), we have a plan to apply this technique to observe Jovian auroral radiation reflected on icy moons. For feasibility studies, we derived an expanded radar equation for planetary radio waves reflected on the moon's surface, including the loss due to the moon's spherical shape and scattering by surface roughness. Using this equation, we estimated the power and polarization characteristics of reflected radio emissions in two cases; terrestrial auroral kilometric radiation (AKR) reflected on the lunar surface and Jovian Hectometric radiation (HOM) reflected on the Ganymede surface. We showed the quantitative feasibility of the observation capability and potential of polarization measurements for

detecting the permittivity of a surface. Additionally, we compared the estimation of the lunar case with a real case of AKR reflection observed using Lunar Radar Sounder (LRS) aboard Kaguya. The observed power ratio of reflected AKR to incident one was 2-5%, estimated from the interference fringe in the observed frequency-time diagram. This observed value agreed with the estimation from our radar equation.

Keywords

passive radar sounding, planetary radio emission, Moon, Ganymede, icy moons, JUICE, Kaguya

1. Introduction

Radar sounding is one of the remote sensing tools for exploring the surfaces of planetary objects. There are two types of radar observations: active and passive. While active radar uses self-emitted radio waves, passive radar utilizes reflections of natural radio waves. It potentially contributes to simplifying instruments without emitting strong radio waves from spacecraft.

For some planets, passive radar can utilize strong planetary auroral radio waves such as auroral kilometric radiation (AKR, several hundreds of kHz) from Earth, decametric (DAM, several tens of MHz), hectometric (HOM, several MHz), and kilometric (KOM, several hundreds of kHz) radiations from Jupiter. Additionally, solar radio bursts from hundreds of kHz to tens of MHz can also be used. These include long wavelength waves not easily transmitted from spacecraft with short antennas; therefore. This technique can provide complementary information to active radar observations and other remote sensing tools. Furthermore, passive radar also has the capability to sound objects with a variety

of reflection angles because the locations of the radio source (a transmitter) and spacecraft (a receiver) differ. This enables us to evaluate permittivity from the dependence of reflected power on reflection angle.

Using Radio and Plasma Wave Investigations (RPWI) aboard the Jupiter Icy Moons Explorer (JUICE), we will try to apply this technique for sounding Jovian icy moons during flybys and on the orbit around Ganymede (Kumamoto et al. 2018; Wahlund et al. 2025). The high-frequency part of the RPWI can observe Jovian auroral radio emissions from ~20 kHz to ~40 MHz with its three-axis electric field antenna, which provides first direction finding and polarization capabilities in the Jovian orbit. We use this for the studies of Jovian radio activities, the ionospheric structures of icy moons using the limb occultation of Jovian auroral radiation (Yasuda et al. 2024), and passive radar sounding of icy moons (Kumamoto et al. 2018). The RIME aboard JUICE and REASON aboard Europa Clipper are also planning this method (Schroeder et al. 2016). We implemented two types of passive radar sounding. If auroral radiation is highly variable, reflected planetary radio waves can be identified as delayed echo signals in autocorrelation analysis. If radiation is coherent and continuous, reflected planetary radio waves create an "interference pattern" that appears in a frequency-time spectrogram, caused by differences in the resonance between incident waves from the source and reflected waves from the moon's surface (Ono et al. 2010). As for passive radar based on RPWI, Kumamoto et al. (2018) discussed the latter case for ideal specular reflection of Ganymede's surface.

In addition to Kumamoto et al. (2018), in this paper, we establish an expanded radar equation as a feasibility study tool for passive radar on our own, which includes the loss due to the moon's spherical shape (Romero-Wolf et al. 2015), surface scattering due to

roughness (Schroeder et al. 2016), and partial reflection which depends on the effective permittivity of a surface. We apply this tool to estimate the power and polarization characteristics of reflected waves in two cases; terrestrial AKR reflected from the lunar surface and Jovian Hectometric radiation (HOM) reflected on the Ganymede surface. Finally, we evaluate the AKR reflected on the Moon with the Kaguya LRS observations in 2007, and provide the first quantitative evaluation of the passive radar sounding on the planetary objects.

2. Passive radar equation for a spherical object with perfect reflection without scattering

Passive radar uses radio waves from a distant radio source and detects the reflected waves. For a spherical object with perfect reflection, the flux density of reflected waves observed at spacecraft, X_{ref}, is expressed by the passive radar equation as follows:

$$X_{ref} = g_{sp}\, g_{sc}\, X_{in} \quad (1)$$

X_{in} is flux density of incident waves assumed as plane waves; this flux density is constant on a spherical surface because incident waves are propagated from a distant source. g_{sp} is the spherical factor, which represents the geometric spreading loss due to reflection on a spherical surface. g_{sc} is the scattering factor, another geometric spreading loss due to surface scattering.

Initially, we use the case with perfect reflection without surface scattering ($g_{sc} = 1$) and derive the spherical factor g_{sp}. **Figure 1** shows the schematic view of this case. The radio source is located along the z-axis. We define two angles of the reflection point on the surface, a sub-source angle θ and an azimuth angle ϕ, as the angle to the incident radio source (z-axis). S_0 is a small area on the surface illuminated by radio waves. The

spherical factor can be defined as follows:

$$g_{sp} = \frac{S_{in}}{S_{ref}} = g_{sp_\theta}\, g_{sp_\phi} \qquad (2)$$

S_{in} is the area perpendicular to the optical axis, where incident waves illuminates S_0. S_{ref} is that illuminated by reflected waves. In this case, we can define the spherical factor g_{sp_θ} along θ and g_{sp_ϕ} along ϕ.

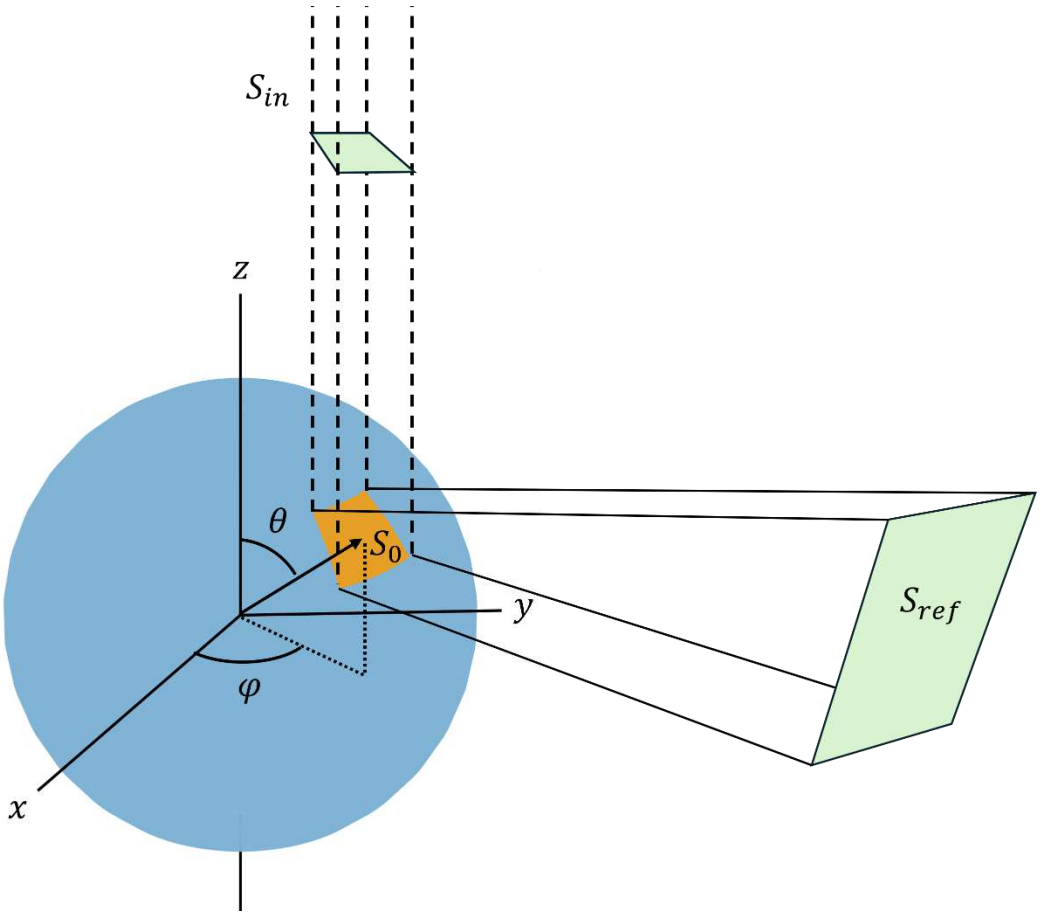


Figure 1. Schematic view of the geometry for the spherical factor, g_{sp}

2.1 Spherical factor along the sub-source angle (g_{sp_θ})

Figure 2 illustrates the meridional cross section of **Figure 1** at S_0. **Figure 2(A)** shows two incident waves that have the incident angles of θ and $\theta + \Delta\theta$ and reflect on a

sphere with a radius of R at Q_1 and Q_2, respectively, corresponding to the latitudinal edges of the reflection area S_0. $\Delta\theta$ is the difference in the latitude between Q_1 and Q_2. The distance between Q_1 and Q_2 is $R\Delta\theta$. As shown in **Figure 2(B)**, the difference in the angles of reflected waves at Q_1 and Q_2 is $2\Delta\theta$. Both waves merge at "the focus point" P_f. R_f is the distance from the reflection point Q_1 to P_f. Focusing on green triangle in **Figure 2(B)**, the interior angles at P_f, Q_1, and Q_2 are expressed as $2\Delta\theta$, $\frac{\pi}{2}+\theta$, and $\frac{\pi}{2}-2\Delta\theta-\theta$, respectively. R_f can be derived using the law of sines, as follows:

$$\frac{R\Delta\theta}{\sin 2\Delta\theta} = \frac{R_f}{\sin\left(\frac{\pi}{2}-\theta-2\Delta\theta\right)} \tag{3}$$

$$R_f = \frac{1}{2}R\cos\theta \qquad \text{in } \Delta\theta \to 0 \tag{4}$$

The distance from spacecraft at the sub-source angle α and height H to the reflection point (L in **Figure 2(C)**) is expressed as follows:

$$L = \sqrt{2R(1-\cos(\alpha-\theta))(R+H)+H^2} \tag{5}$$

$$\alpha = 2\theta - \sin^{-1}\left(\frac{R}{R+H}\sin\theta\right) \tag{6}$$

In this geometry, g_{sp_θ} is the ratio of the distance from P_f to Q_1 (=R_f) to the distance from P_f to spacecraft (= $R_f + L$), obtained as follows using equations (4), (5), and (6):

$$g_{sp_\theta} = \frac{R_f}{R_f+L} = \frac{R\cos\theta}{R\cos\theta+2L} \tag{7}$$

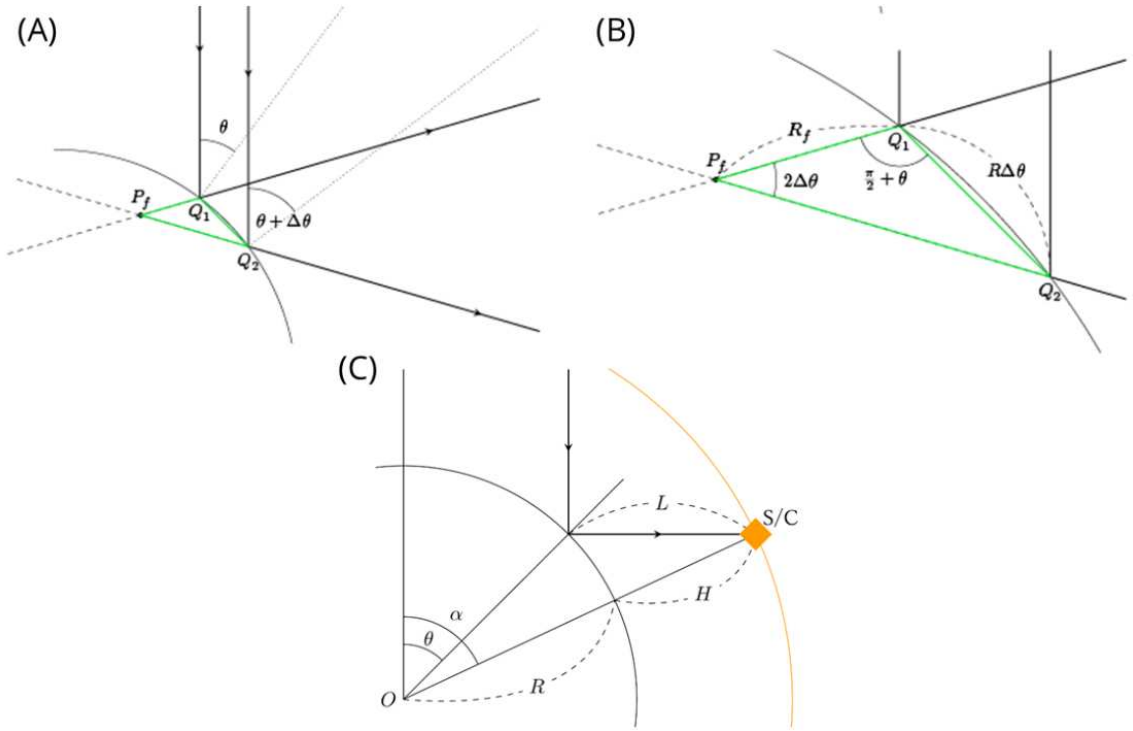


Figure 2. Geometry of incident and reflected waves related to sub-source angle. Waves are reflected at sub-source angle (θ), and observed at sub-source angle α and height H.

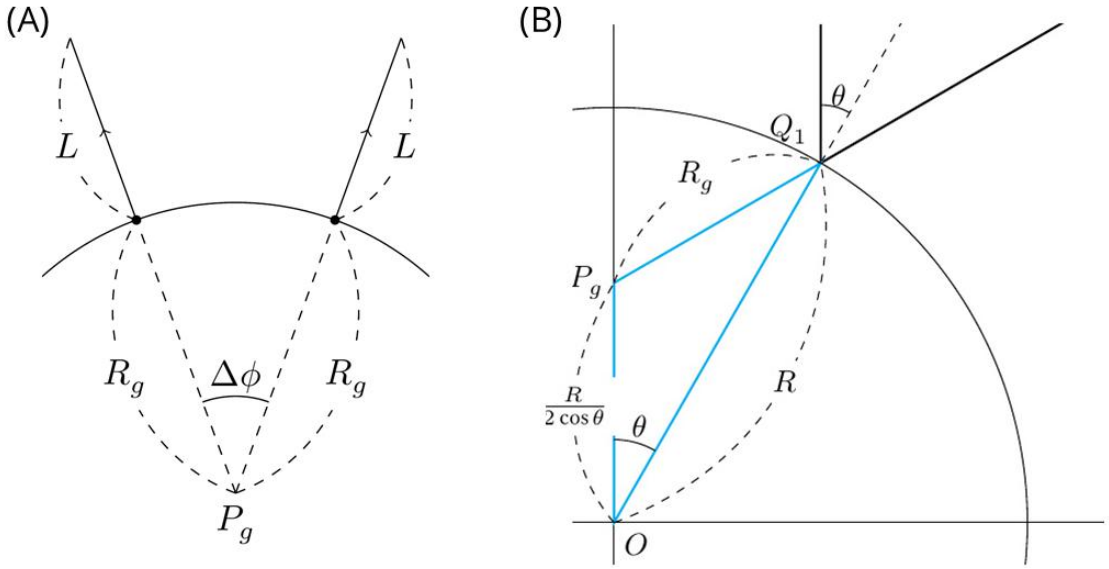


Figure 3. Geometry related to azimuth angle (ϕ). (A) A view from the radio source (+Z). (B) A view from the perpendicular direction, same as that in Figure 2.

2.2 Spherical factor along azimuthal angle (g_{sp_ϕ})

Figure 3 also shows the light path of radio waves with an incident sub-source angle of θ. **Figure 3(A)** displays the view from the radio source (+Z). Two reflection points shown by black dots correspond to the longitudinal edges of the reflection area S_0. **Figure 3(B)** of the view perpendicular to the incident plane. Because of axial symmetry, reflected waves merged at the focus point P_g on Z-axis. Here, we focus on blue triangle in **Figure 4(B)**. The distance P_g from the center of the spherical object, OP_g, is expressed as follows:

$$OP_g = \frac{R}{2\cos\theta} \tag{8}$$

From the law of sins, the distance between the reflection point and focus point, R_g, is as follows.

$$R_g = \frac{R}{2\cos\theta} \tag{9}$$

In this geometry, using L in equations (5) and (6), g_{sp_ϕ} is the ratio of $R_g\Delta\phi$ to $(R_g + L)\Delta\phi$, and the geometric spreading loss along ϕ is defined as follows:

$$g_{sp_\phi} = \frac{R_g\Delta\phi}{(R_g+L)\Delta\phi} = \frac{R_g}{R_g+L} = \frac{R}{R+2L\cos\theta} \tag{10}$$

2.3 Comparison of the passive radar equation with ray tracing

From equations (2), (7) and (10), we derived the spherical effect g_{sp} for the spacecraft at the sub-source angle of α and the height of H as following:

$$g_{sp} = \frac{R\cos\theta}{R\cos\theta+2L}\,\frac{R}{R+2L\cos\theta} \tag{11}$$

We verify the passive radar equation (equation (1)) with this value from ray tracing. **Figure 4** shows an example of ray tracing in cross-section at y=0. Incident waves are injected from the +Z direction. The reflection sphere has a radius of 1.

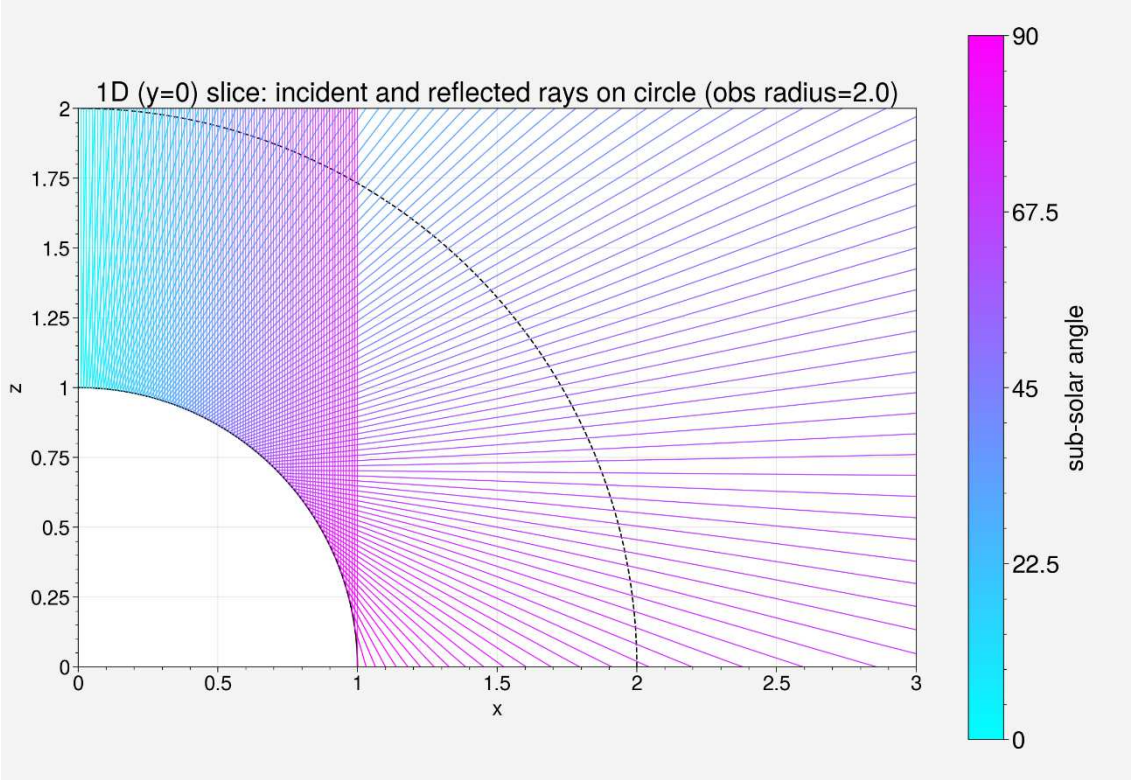


Figure 4. Incident and reflected rays in a ray trace study of a spherical object with a radius of 1. Dotted circle shows the spacecraft orbit at a height of 2.0.

We uniformly set 5000×5000 of incident rays in x = 0–1 and y = 0–1. At a specific spacecraft height ($R_{obs} = 2$ in the case shown in **Figure 4**), we count the number of reflected rays per the area (dS), which covers $\Delta\theta$ = 1° along the sub-source angle θ and $\Delta\phi$ = 1° along the azimuth angle ϕ. This value is divided by the area $dS = R_{obs}^2 \sin\theta$ for conversion to the number per the solid angle of $1° \times 1°$. Since dS is perpendicular to the vector from the sphere center to spacecraft, it is not perpendicular to the optical axis of reflected waves. Therefore, we divide this value by $\cos\beta$, where β is the angle between the sphere's normal vector and reflected wave's vector. After these corrections, we obtain the flux of reflected rays on the plane perpendicular to the reflected wave vector.

Using these results, we evaluate the ratio of reflected and incident waves in the Moon

(R = 1,737 km) and Ganymede (R = 2,634 km). The spacecraft heights are assumed to be 1, 100, 200, 500, and 1,000 km. **Figure 5** shows the results from the radar equation and ray tracing for the (A) Moon and (B) Ganymede cases. The horizontal axis is the sub-source angle of spacecraft (α). The vertical axis is the power ratio of reflected wave to incident wave. We confirm that the results of the radar equation (dotted line) and ray trace (solid lines) match perfectly.

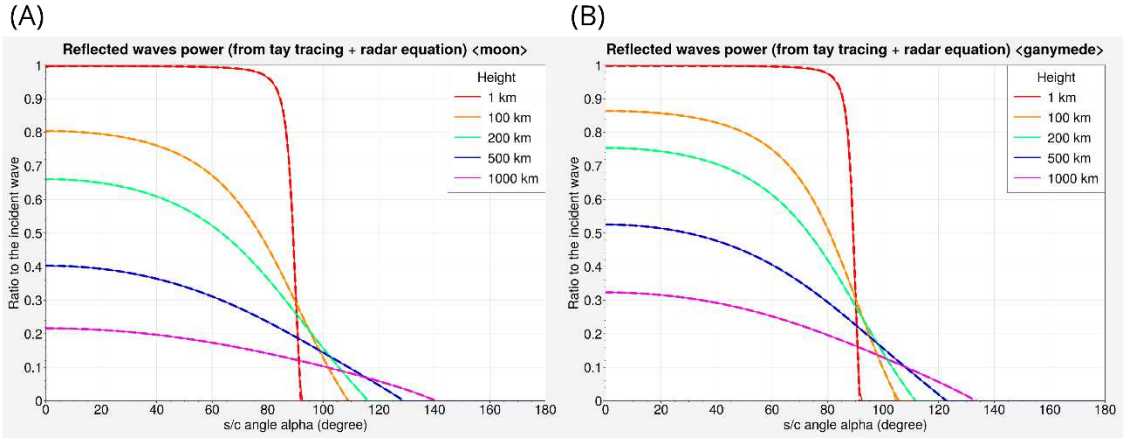


Figure 5. Power ratio of a reflected wave to an incident wave derived by the radar equation (dotted lines) and ray tracing (solid lines) at spacecraft with the heights of 1 (red), 100 (orange), 200 (green), 500 (blue), and 1,000 km (purple): (A) Moon radius case and (B) Ganymede radius case.

3. Radar equation with surface scattering and partial reflection

3.1 Surface scattering effect

Next, we consider reflection with surface scattering. **Figure 6** shows the geometry of plane reflection with scattering, modified from Figure 2 of Schroeder et al. (2016). As Schoeder et al. (2016), we introduce the "scattering angle" σ_s, which is the spread angle of reflection wave due to scattering at a surface with roughness. On a surface with no roughness, σ_s is 0. On a surface with roughness, we assume that the reflection angle is

uniformly spread with $\pm\sigma_s$. The scattering factor g_{sc} the geometric spreading loss due to scattering on a surface is defined as the ratio of the area illuminated at the surface (A_1) to that at the spacecraft at a distance of L (A_2):

$$g_{sc} = \mathrm{A}_1/\mathrm{A}_2 = \pi {F_1}^2/\pi {F_2}^2 \quad (12)$$

where F_1 and F_2 are the radii of A_1 and A_2, respectively.

F_1 is set as the Fresnel radius, the range on the surface wherein a radio wave can illuminate the same phase (Schroeder et al. 2016). It is expressed as follows:

$$F_1 = \sqrt{\frac{r_1 r_2 \lambda}{r_1 + r_2}} \quad (13)$$

where r_1 is the distance from the surface to the incident radio source, r_2 is the distance from the surface to spacecraft, and λ is the wavelength of radio waves. In the passive radar case, the source is far enough to assume that $r_1 \gg r_2$; equation (13) becomes as follows:

$$F_1 \simeq \sqrt{L\lambda} \quad (14)$$

Then, F_2 at a distance of L with a scattering angle of σ_s is defined as follows:

$$F_2 = F_1 + L\tan\sigma_s = \sqrt{L\lambda} + L\tan\sigma_s \quad (15)$$

From equations (12), (14), and (15), the scattering factor g_{sc} is expressed as follows:

$$g_{sc} = \frac{1}{\left(1+\sqrt{\frac{L}{\lambda}}\tan\sigma_s\right)^2} \quad (16)$$

Equation (16) is the same as Equation (17) in Schroeder et al. (2016) for the nadir illumination case. We also apply this for oblique incidence cases.

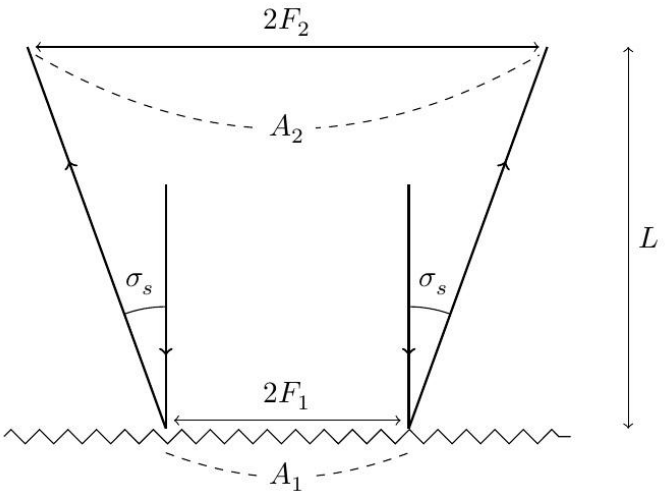


Figure 6. Geometry of plane reflection with respect to the scattering angle (σ_s).

3.2 Partial reflection effect

A real surface has finite permittivity, ε, and shows partial reflection. It depends on surface permittivity and the angle and polarization of incident waves. We separately consider the TE mode with the electric field perpendicular to the incident plane and TM mode with the magnetic field perpendicular to the incident plane. From Snell's law and boundary conditions for electromagnetic waves, the power reflectance of the TE mode (R_{TE}) and TM mode (R_{TM}) are expressed as follows:

$$R_{TE} = \left(\frac{\cos\theta_{in} - \sqrt{\varepsilon - \sin^2\theta_{in}}}{\cos\theta_{in} + \sqrt{\varepsilon - \sin^2\theta_{in}}}\right)^2 \quad (17)$$

$$R_{TM} = \left(\frac{\varepsilon\cos\theta_{in} - \sqrt{\varepsilon - \sin^2\theta_{in}}}{\varepsilon\cos\theta_{in} + \sqrt{\varepsilon - \sin^2\theta_{in}}}\right)^2 \quad (18)$$

Figure 7 shows the power reflectance on the surface at various incident angles of (A) Moon and (B) Ganymede. As in previous studies, we assume that the permittivity of the Moon is from ~6 (rock, low porosity case) (Hongo et al. 2020) and that of Ganymede is ~3 (ice) (Fujita et al. 2000). The TM mode shows Brewster's angle where the reflectance is 0. It depends on the effective permittivity of the surface. This suggests that polarization

of passive radio sounding with wide sub-source angles is important. This will be discussed again on Sec. 5.

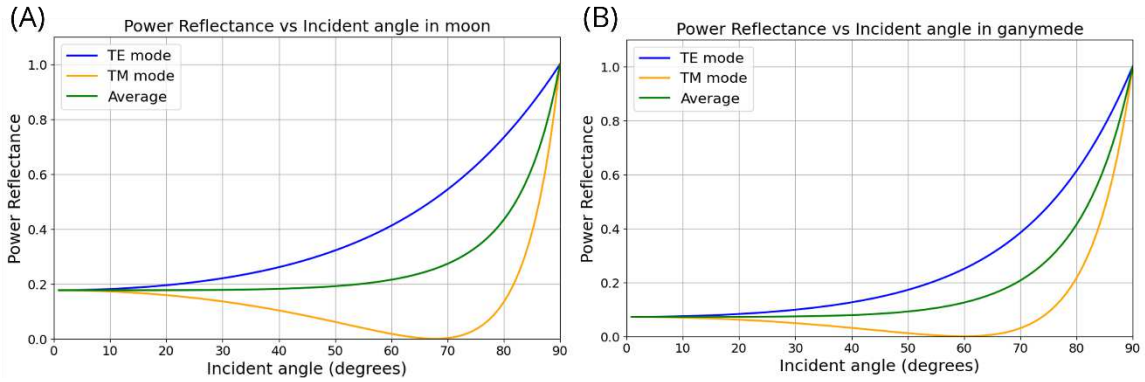


Figure 7. Reflectance on the surface at various incident angles for the TE mode (blue), TM mode (orange), and average (green): (A) ε=6 (Moon, rock) and (B) ε=3 (Ganymede, ice).

4 Estimated power of planetary radiation reflected on Moon and Ganymede

We combine all effects described in **Sections 2** and **3** and evaluate the power of planetary auroral radio waves reflected on the Moon and Ganymede. For the former, we have the data of AKR reflected on the lunar surface observed by Kaguya (ex. Figure 22 in Ono et al. (2010)). For the latter, we plan to observe Jovian auroral radiation reflected on Europa, Ganymede, and Callisto (e.g., Sec. 3.3 in Wahlund et al. (2025)).

Figure 8 shows the power ratio of a reflected wave to an incident wave as a function of sub-planet angles of spacecraft in the circular orbit. Panels **A** and **B** show the TE mode, Panels **C** and **D** are the TM mode, and Panels **E** and **F** are their average. Left panels **(A**, **C**, and **E)** show the Moon case (R = 1,737 km) with ε~6, which is a lower porosity case of the rocky surface (Hongo et al. 2020). Planetary radiation is assumed to be AKR with a wavelength of 1 km (300 kHz). Right panels **(B**, **D**, and **F)** show the Ganymede case (R = 2,634 km) with ε~3 based on the icy surface (Fujita et al. 2000). Planetary radiation is assumed to be hectometric radiation (HOM) with a wavelength of 100 m (3 MHz). All

panels show the expected ratio at heights of 100 (orange), 500 (blue), and 1,000 km (purple), with scattering angles σ_s of 0° (solid), 1° (dashed), and 2° (dotted), respectively. (Note: The real angle between the planetary center and radio source is ~2° from the Moon for AKR at 300 kHz and ~8° from Ganymede for HOM at 3 MHz.)

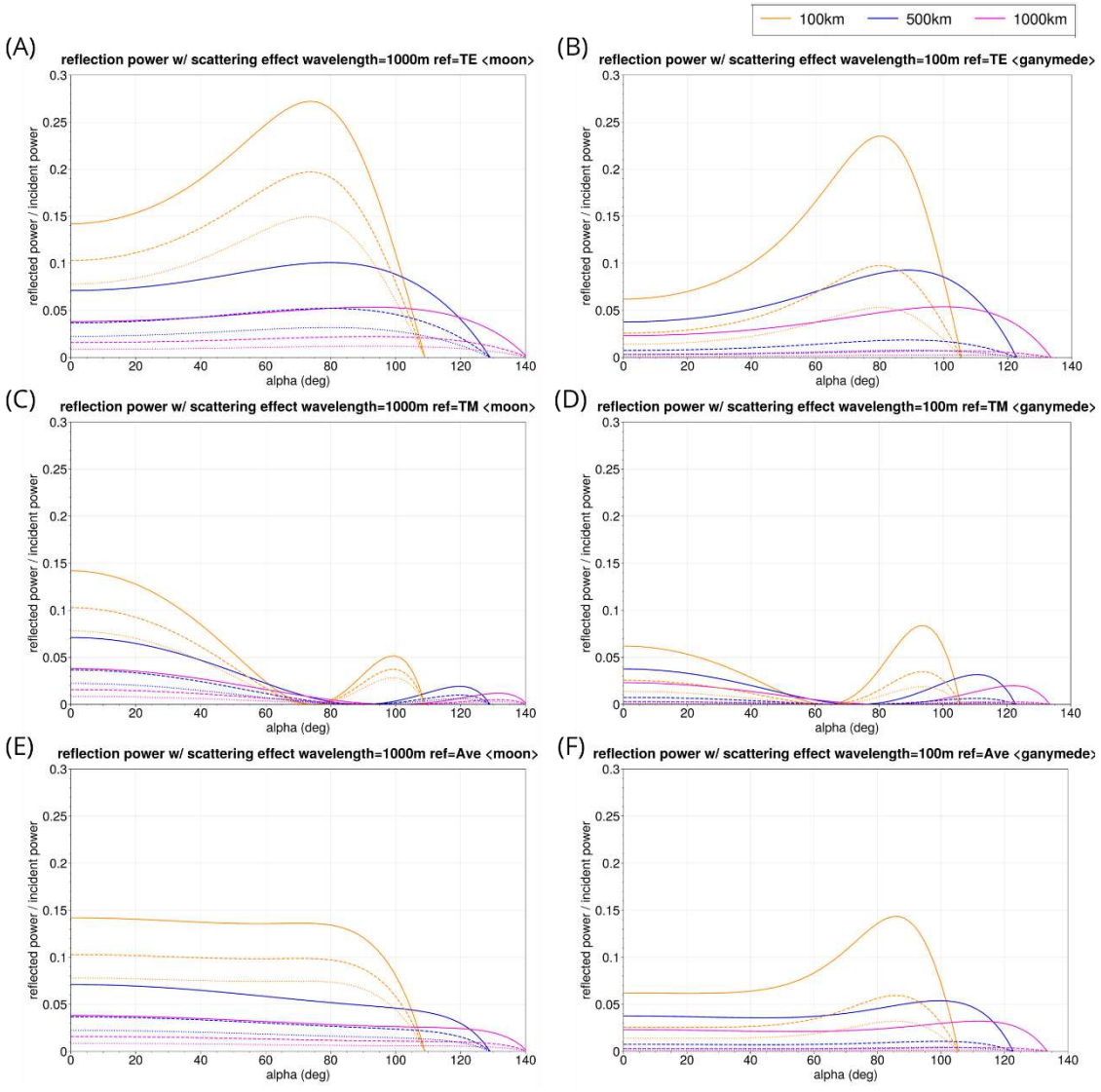


Figure 8. Expected power ratio of a reflected wave to an incident wave in (A)(B) TE mode, (C)(D) TM mode, and (E)(F) their average. Left panels (A), (C), and (E) are the Moon case at 300 kHz for AKR. Right panels (B), (D), (F) are the Ganymede case at 3 MHz for HOM. Observed height is 100 (orange), 500 (blue), and 1,000 km (purple). Scattering angle is 0° (solid), 1° (dashed), and 2° (dotted).

Figure 8 shows that altitude is important for detection. At a height of 100 km, the power ratio of a reflected wave to an incident wave in the nadir view ($\alpha = 0°$) ranges from ~15% to ~10% in the Moon case and from ~7% to ~3% in the Ganymede case. These values become 1/2 at a height of 500 km, and ~1/4 at a height of 1,000 km. The reflectance is lower on the icy surface with a lower ε than that on the rocky surface with a higher ε. (This fact potentially enhances the possibility of detecting a subsurface under an icy surface because of higher transmittance into the sub-surface. However, this paper does not discuss the passive subsurface sounding capability discussed by Kumamoto et al. (2018).)

The effect of the scattering loss affects larger in the Ganymede case. This is because the Ganymede case uses 3 MHz, which is 10 times higher frequency than the Moon case (300 kHz). A shorter wavelength leads to a smaller Fresnel radius and results in a higher scattering loss as shown in Equation (16). We will take care of this effect in future JUICE RPWI observations.

Furthermore, **Figure 8** shows the importance of polarization measurement at higher sub-planet angles. In the TE mode (**Figures 8(A)** and **8(B)**), because of the effect of enhanced reflectance shown in **Figure 7**, the ratio of reflected waves is not lower or more enhanced even in a region close to or beyond the limb (~90°). In the TM mode (**Figures 8(C)** and **8(D)**), reflected waves are zero at Brewstar's angle, $68°$ in $\varepsilon \sim 6$ for the Moon case and $60°$ in $\varepsilon \sim 3$ for the Ganymede case. This is a merit of passive radar sounding which can observe reflectance with wide sub source angles. Although the observed polarization is a mixture of incident and reflected waves, careful analyses have a potential to measure surface permittivity which reflects both composition and porosity.

5. Evaluation with a case of reflected AKR on the Moon observed by Kaguya

AKR reflectance on the lunar surface can be derived from the observation data from Lunar Radar Sounder (LRS) aboard the JAXA Kaguya orbiter. The data show interference fringes in the frequency-time diagram, as shown in **Figure 9(A)** (Figure 22(b) of Ono et al. (2010)), from 20:52 to 20:57 on November 22, 2007. **Figure 9(B)** shows the sub-Earth angle of Kaguya. The height of Kaguya from the lunar surface is ~90 km (90 km at 20:52 and 89 km at 20:57).

In the continuous AKR spectra, the interference pattern can be created by the difference in the light path length (ΔL) between direct waves from the Earth and reflected waves from the lunar surface. The wave strength is maximum at frequency f where $f\,\Delta L/c$ is an integer (c: light speed); thus, the interval of fringes Δf is $c/\Delta L$.

In these data, Kaguya moved from the Earth side to the opposite above the polar region with a sub-Earth angle of ~$91°$ at 20:52 to ~$105°$ at 20:57. The Kaguya LRS antenna was tangential to the lunar surface during this observation; therefore, we assume that reflected waves are mainly in the TE-mode. Kaguya is close to the limb, and incident and reflected waves will gradually become parallel. Therefore, the difference in the light path ΔL is gradually reduced, and the interval of fringes Δf becomes gradually wider. With the frequency resolution of Kaguya (6 kHz), LRS could resolve the interference after ~20:52. (this resolution cannot resolve narrower fringes at lower sub-Earth angles.)

Since electric field vectors of incident waves are close to parallel to those of reflect waves, we assume that the observed amplitude of the electric field is modulated as $E_{in} \pm E_{ref}$, where E_{in} and E_{ref} are the amplitudes of incident and reflected AKR, respectively. From this modulation, we try to derive the reflectance at the surface. The maximum (P_{out+}) and minimum (P_{out-}) powers of the fringe are as follows:

$$P_{out+} = \varepsilon_0 \left(E_{in} + E_{ref}\right)^2 \quad (19)$$

$$P_{out-} = \varepsilon_0 \left(E_{in} - E_{ref}\right)^2 \quad (20)$$

ε_0 is the vacuum permittivity. Using the power reflectance R_{TE}, E_{ref} is as follows:

$$E_{ref} = \sqrt{R_{TE}}\, E_{in} \quad (21)$$

With equations (19), (20) and (21), the modulation ratio of the observed fringe, P_{out+}/P_{out-}, is expressed as follows:

$$\frac{P_{out+}}{P_{out-}} = \frac{\varepsilon_0 \left(E_{in} + \sqrt{R_{TE}}\, E_{in}\right)^2}{\varepsilon_0 \left(E_{in} - \sqrt{R_{TE}}\, E_{in}\right)^2} = \frac{\left(1+\sqrt{R_{TE}}\right)^2}{\left(1-\sqrt{R_{TE}}\right)^2} \quad (22)$$

Therefore, the power reflectance R_{TE} is expressed based on the observed power modulation ratio A [dB] as follows:

$$R_{TE} = \left(\frac{10^{A/20} - 1}{10^{A/20} + 1}\right)^2 \quad (23)$$

In this observation, we use the data in red squares in **Figure 9(A)**: around (i) 20:53 and (ii) 20:54, at the sub-Earth angles of (i) ~94° and (ii) ~96°, respectively. The corresponding modulation ratios are (i) 4.18 ± 0.83 dB, (ii) 2.64 ± 0.71 dB. From equation (23), the corresponding power ratios of a reflected wave to an incident wave are derived as (i) ~0.056 (0.037–0.079), and (ii) ~0.023 (0.012–0.036)

These results are compared with estimation from the radar equation, assuming effective permittivity and scattering on the lunar surface. **Figure 10** shows the power ratio of a reflected wave to an incident wave for the Moon at the Kaguya height, ~100 km. The case of ε ~ 6 is from **Figure 8(A)**. We also add the cases of ε ~ 3 (the lower porosity case of Hongo et al. (2020)) with a larger scattering angle of 4°. Dashed red crosses and squares show values derived from the Kaguya observations.

The observed power ratio is slightly lower than that in the case of ε~3 and a scattering

angle of ~4°. According to the global elevation data from Lunar Orbiter Laser Altimeter (Pommerol et al. 2012), the differential slope of the lunar surface is 1°- 2° in the highland at the 10 km baseline which is close to the Fresnel radius of AKR in 100s kHz. Based on this roughness value, we apply a scattering angle of ~4° in **Figure 10** because the scattering angle for plane waves can be assumed as twice of the differential slope angle. This result supports that the radar equation established in this study agrees with the observations and it is possible to be utilized for feasibility studies of future passive radio sounding, including the icy moon observations planned by JUICE RPWI.

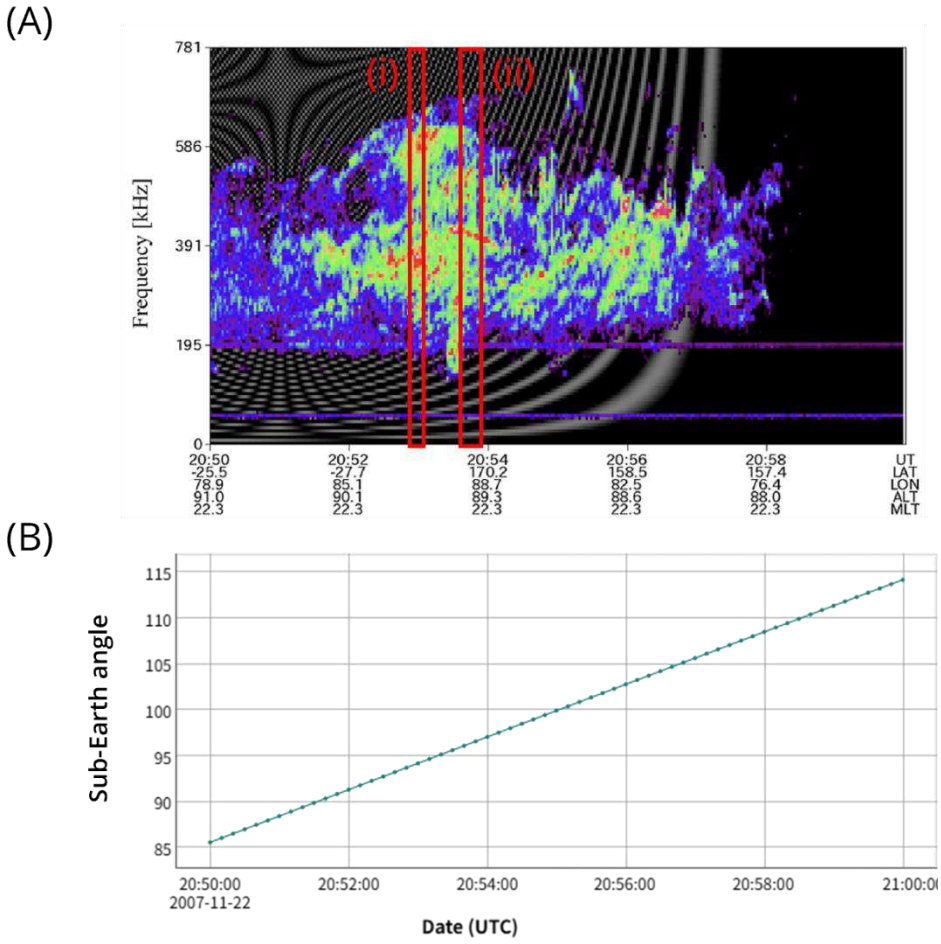


Figure 9. Spectrogram of AKR with interference patterns observed by Kaguya LRS on 22 November 2007 above the lunar polar region. (A) AKR spectrogram with the calculated phase difference between direct waves from the Earth and waves reflected on the lunar surface (from Figure 22(b) in Ono et al. (2010)). (B) Sub-Earth angle of Kaguya.

It is noted that JUICE RPWI observed AKR during the Lunar Gravity Assist, at 400 ± 111 kHz with a resolution of 89 Hz from 21:19-21:24 UT on August 19, 2024. We detected polarized AKR with a signal-to-noise ratio of ~20–30 dB at a height of 930–1,530 km and a sub-Earth angle of ~90°. Under those conditions, **Figure 8E** suggests that the power ratio of a reflected wave could be ~1 % or less, and it was hard to distinguish it with autocorrelation nor interference fringes. JUICE's passive sounding of icy moons in the 2030s should try from lower altitudes.

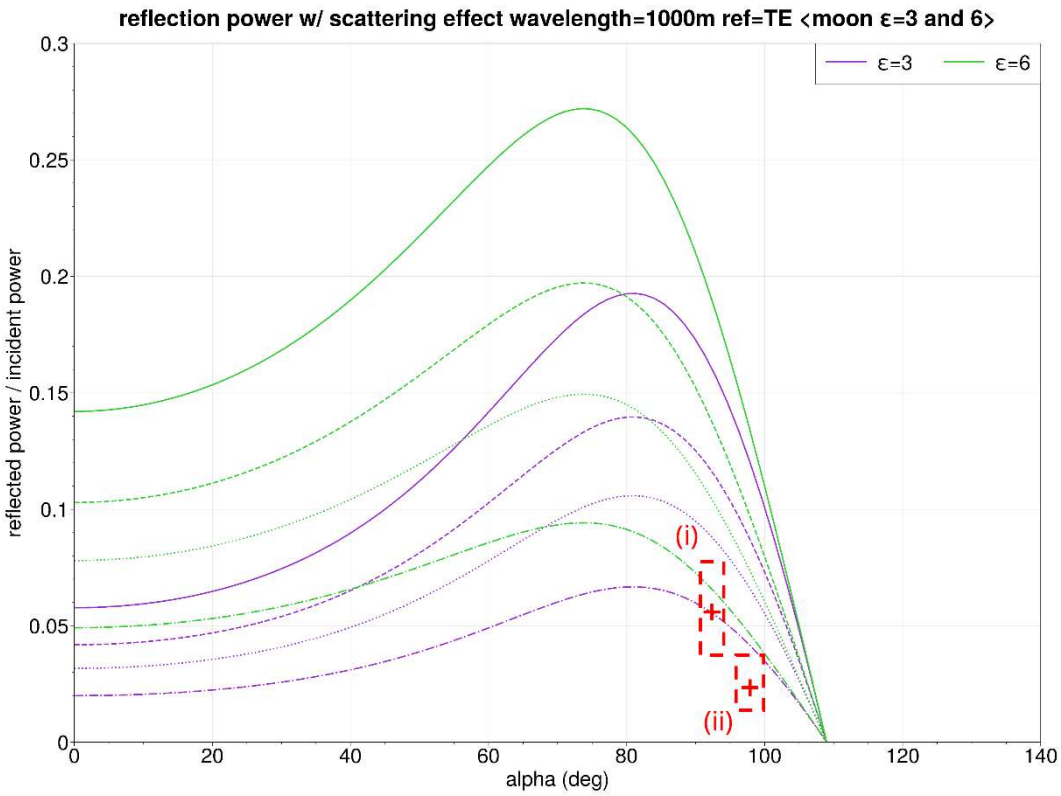


Figure 10. Expected power ratio of reflected to incident AKR in the Kaguya case (height ~ 100 km) in the TE mode, at scattering angles of 0° (solid), 1° (dashed), 2° (dotted), and 4° (dash-dot). Green lines are a lower porosity (ε ~ 6). Purple lines are a higher porosity (ε ~ 3).

6. Conclusion

In this study, we established a radar equation for passive radio sounding observations to be planned by JUICE RPWI for Jovian icy moons. For the spreading loss of reflected waves, we evaluated two factors: the spherical factor g_{sp} and scattering factor g_{sc}. The former is the ratio of spreading of waves reflected on a spherical surface, which was confirmed via ray tracing studies. For the latter, we used the spread angle of reflection due to scattering (Schroeder et al. 2016). Additionally, we included the Fresnel reflectance linked to the effective surface permittivity including porosity. Combining these factors, we estimated the ratio of a reflected wave to an incident wave, which depended on the sub-source angle and spacecraft height.

We used the developed tool and evaluated the power and polarization characteristics of reflected radio waves for two cases: AKR reflected on the lunar rocky surface ($\varepsilon \sim 6$) and Jovian radio emissions (HOM) reflected on the Ganymede's icy surface ($\varepsilon \sim 3$). We emulated spacecraft heights of 100, 500, and 1,000 km, and the scattering angles of $0°$, $1°$, and $2°$, in the TE mode, TM mode, and their average. The results showed the quantitative feasibility of passive radar sounding and showed the potential of polarization measurements at large sub-source angles to detect the effective surface permittivity from Brewster's angle.

Finally, we compared the Moon's case with a Kaguya LRS measurement of AKR reflected on the lunar surface. From interference fringes in the frequency-time diagram, we estimated the power ratio of reflected AKR to the incident one as 0.023-0.056. The estimated value from the radar equation agreed with the observed value. The tool established in this study will be used for feasibility studies of future passive radio sounding including icy moon observation planned by JUICE RPWI.

List of abbreviations

AKR	auroral kilometric radiation
JAXA	Japan Aerospace Exploration Agency
JUICE	Jupiter Icy Moons Explorer
LRS	Lunar Radar Sounder
RPWI	Radio and Plasma Investigations

Declarations

Ethics approval and consent to participate

Not applicable.

Consent for publication

Not applicable

Availability of data and materials

Kaguya LRS/NPW data is from JAXA DARTS (https://darts.isas.jaxa.jp/datasets/darts:sln-l-lrs-5-npw-spectrum-v1.0).

Kaguya orbit data is from JAXA WebGeoCalc (https://darts.isas.jaxa.jp/webgeocalc/).

Competing interests

The authors declare no competing interests.

Funding

This study was supported by Japan Aerospace Exploration Agency (JAXA), as a part of the contribution to the JUICE mission from Japan.

Authors' contributions

A. Kawakami derived the radar equations, executed whole analyses, and wrote this paper as the main author. Y. Kasaba directed and supported this study as Co-PI of JUICE RPWI. A. Kumamoto provided the basis of radar studies and supported the data analyses of Kaguya LRS. F. Tsuchiya implemented and supported the passive radar capability of JUICE RPWI. Emi Tanaka analyzed the Kaguya LRS data and estimated the reflectance of the lunar surface. Y. K. and F. T. also supported editing all text and figures in this paper.

Acknowledgements

We gratefully acknowledge J.-E Wahlund, Baptiste Cecconi, and all colleagues who have contributed to the high frequency part of the JUICE RPWI. We express our sincere thanks to all the JUICE project members for their careful work.

References

Fujita S, Matsuoka T, Ishida T, Matsuoka K, Mae S (2000) A summary of the complex dielectric permittivity of ice in the megahertz range and its applications for radar sounding of polar ice sheets. *Physics of Ice Core Records* 185–212. https://www.semanticscholar.org/paper/A-summary-of-the-complex-dielectric-permittivity-of-Fujita-Matsuoka/f034ded2d8f41fd8892e5010d140d08936fa53ce

Hongo K, Toh H, Kumamoto A (2020) Estimation of bulk permittivity of the Moon's

surface using Lunar Radar Sounder on-board Selenological and Engineering Explorer. *Earth, Planets and Space* 72 137. https://doi.org/10.1186/S40623-020-01259-2

Kumamoto A, Kasaba Y, Tsuchiya F, Misawa H, Kita H, Puccio W, Wahlund J.-E, Bergman J, Cecconi B, Goto Y, Kimura J, Kobayashi T (2018) Feasibility of the exploration of the subsurface structures of Jupiter's icy moons by interference of Jovian hectometric and decametric radiation. Planetary Radio Emissions VIII, 127-136, ed. G. Fischer, G. Mann, M. Panchenko, and P. Zarka, Austrian Academy of Sciences Press, Vienna. https://doi.org/10.1553/PRE8s127

Ono T, Kumamoto A, Kasahara Y, Yamaguchi Y, Yamaji A, Kobayashi T, Oshigami S, Nakagawa H, Goto Y, Hashimoto K, Omura Y, Imachi T, Matsumoto H, Oya H (2010) The Lunar Radar Sounder (LRS) Onboard the KAGUYA (SELENE) Spacecraft. *Space Science Reviews* 154 145–192. https://doi.org/10.1007/S11214-010-9673-8

Pommerol A, Chakraborty S, Thomas N (2012) Comparative study of the surface roughness of the Moon, Mars and Mercury. *Planet Space Science* 73 287–293. https://doi.org/10.1016/J.PSS.2012.08.020

Romero-Wolf, A., Vance, S., Maiwald, F., Heggy, E., Ries, P., & Liewer, K. (2015). A passive probe for subsurface oceans and liquid water in Jupiter's icy moons. *Icarus*, *248*, 463–477. https://doi.org/10.1016/J.ICARUS.2014.10.043

Schroeder DM, Romero-Wolf A, Carrer L, Grima C, Campbell BA, Kofman W, Bruzzone L, Blankenship DD (2016) Assessing the potential for passive radio sounding of Europa and Ganymede with RIME and REASON. *Planet Space Science* 134 52–60. https://doi.org/10.1016/J.PSS.2016.10.007

Wahlund JE, Bergman JES, Åhlén L, Puccio W, Cecconi B, Kasaba Y, Müller-Wodarg I, Rothkaehl H, Morawski M, Santolik O, Soucek J, Grygorczuk J, Wisniewski L, Henri P, Rauch JL, Le Duff O, Retinò A, Mansour M, Stverak S, et al. (2024). The Radio and Plasma Wave Investigation (RPWI) for the JUpiter ICy moons Explorer (JUICE). *Space Science Reviews* 221:1. https://doi.org/10.1007/S11214-024-01110-0

Yasuda, R., Kimura, T., Misawa, H., Tsuchiya, F., Cecconi, B., Kasaba, Y., Satoh, S., Sakai, S., & Louis, C. K. (2024). Ray Tracing for Jupiter's Icy Moon Ionospheric Occultation of Jovian Auroral Radio Sources. *Journal of Geophysical Research: Space Physics*, *129*(6), e2024JA032454. https://doi.org/10.1029/2024JA032454

Supplementary Files

This is a list of supplementary files associated with this preprint. Click to download.

- graphicalabst.png